Spray Coating Experiments: Setups and Methodologies

The latest eBook from Advanced Optical Metrology. Download for free.

Spray Coating Experiments: Setups and Methodologies, is the third in our Thin Films eBook series. This publication provides an introduction to spray coating, three article digests from Wiley Online Library and the latest news about Evident's Image of the Year Award 2022.

Wiley in collaboration with Evident, are committed to bridging the gap between fundamental research and industrial applications in the field of optical metrology. We strive to do this by collecting and organizing existing information, making it more accessible and useful for researchers and practitioners alike.

EVIDENT
OLYMPUS

WILEY

NANO · MICRO small
www.small-journal.com

Heterostructured V-Doped $Ni_2P/Ni_{12}P_5$ Electrocatalysts for Hydrogen Evolution in Anion Exchange Membrane Water Electrolyzers

*Tingwen Zhao, Shuhao Wang, Yibing Li, Chen Jia, Zhen Su, Derek Hao, Bing-jie Ni, Qiang Zhang, and Chuan Zhao**

Regulating the electronic structure and intrinsic activity of catalysts' active sites with optimal hydrogen intermediates adsorption is crucial to enhancing the hydrogen evolution reaction (HER) in alkaline media. Herein, a heterostructured V-doped $Ni_2P/Ni_{12}P_5$ (V–$Ni_2P/Ni_{12}P_5$) electrocatalyst is fabricated through a hydrothermal treatment and controllable phosphidation process. In comparison with pure-phase V–Ni_2P, in/ex situ characterizations and theoretical calculations reveal a redistribution of electrons and active sites in V–$Ni_2P/Ni_{12}P_5$ due to the V doping and heterointerfaces effect. The strong coupling between Ni_2P and $Ni_{12}P_5$ at the interface leads to an increased electron density at interfacial Ni sites while depleting at P sites, with V-doping further promoting the electron accumulation at Ni sites. This is accompanied by the change of active sites from the anionic P sites to the interfacial Ni–V bridge sites in V–$Ni_2P/Ni_{12}P_5$. Benefiting from the interface electronic structure, increased number of active sites, and optimized H-adsorption energy, the V-$Ni_2P/Ni_{12}P_5$ exhibits an overpotential of 62 mV to deliver 10 mA cm^{-2} and excellent long-term stability for HER. The V–$Ni_2P/Ni_{12}P_5$ catalyst is applied for anion exchange membrane water electrolysis to deliver superior performance with a current density of 500 mA cm^{-2} at a cell voltage of 1.79 V and excellent durability.

1. Introduction

Electrocatalytic water splitting powered by solar/wind power offers a promising strategy to generate hydrogen with high purity and is environmentally friendly.[1] Alkaline water electrolysis (AWE) and proton-exchange membrane (PEM) water electrolysis are two commercially available electrocatalytic water splitting techniques, however, large energy consumption in AWE and the use of noble-metal based catalysts in PEM electrolyzers prohibited the wide application of these water electrolysis techniques. Anion exchange membrane (AEM) water electrolyzer combines the merits of AWE and PEM electrolyzers, and is regarded as a promising future water electrolysis technology with notable advantages, including the simple and compact structure and the use of earth-abundant transition metal catalysts.[2,3] However, the development of the AEM electrolyzer is still in its infancy to date. Developing high-efficient and stable electrocatalysts is highly required to improve the current density and energy efficiency of the AEM water electrolyzer.

Between the two half-cell reactions in the AEM water electrolyzer, hydrogen evolution reaction (HER) is more challenging in alkaline media due to its sluggish kinetics. The additional water dissociation step to generate proton (H*) sources results in 2–3 orders of lower activity than that in the PEM electrolyzer.[4] Various transition metal (TM)-based materials have been developed in recent years to improve HER activity in alkaline media, including TM sulfides,[5,6] selenides,[7,8] and phosphides.[9–12] In particular, nickel phosphides have attracted great attention due to their high electronic conductivity and structural diversity. However, pure-phase metal phosphides have relatively large absolute values of Gibbs free

T. Zhao, S. Wang, Y. Li, C. Jia, Z. Su, C. Zhao
School of Chemistry
The University of New South Wales
Sydney, New South Wales 2052, Australia
E-mail: chuan.zhao@unsw.edu.au

The ORCID identification number(s) for the author(s) of this article can be found under https://doi.org/10.1002/smll.202204758.

DOI: 10.1002/smll.202204758

Y. Li
Institute of Smart City and Intelligent Transportation
Southwest Jiaotong University
Chengdu 610097, China

D. Hao, B.-j. Ni
Centre for Technology in Water and Wastewater (CTWW)
School of Civil and Environmental Engineering
University of Technology Sydney
Sydney, NSW 2007, Australia

Q. Zhang
Beijing Key Laboratory of Green Chemical Reaction Engineering and Technology
Department of Chemical Engineering
Tsinghua University
Beijing 100084, China

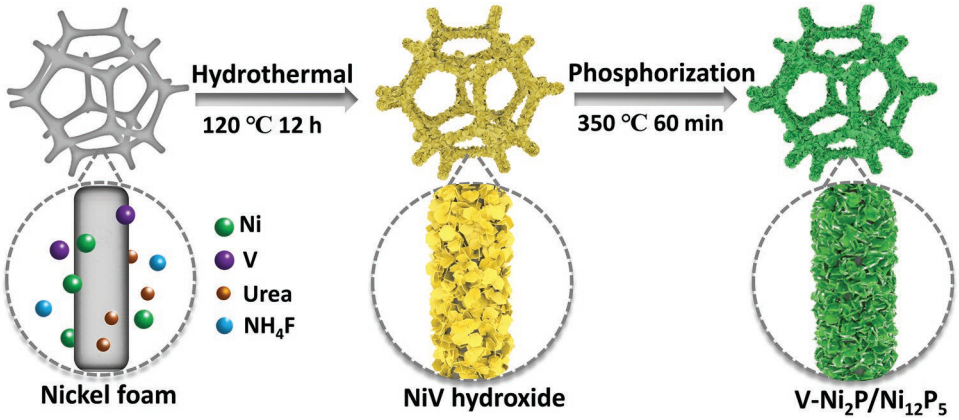

Scheme 1. Illustration for the two-step fabrication of V–$Ni_2P/Ni_{12}P_5$ electrocatalysts.

energy on hydrogen adsorption (ΔG_{H^*}), resulting in strong interaction with hydrogen intermediates, which is unfavorable to overall kinetics.[13] Heterostructured materials have abundant interfaces and optimal structure, which can significantly improve the catalytic activity due to the suitable electronic interactions, optimized band structure, and more exposed active sites.[14] Nickel phosphides-based heterostructured catalysts have been reported, such as $Ni_2P/NiSe_2$,[15] $Ni_2P/NiTe_2$,[16] and NiP_2/FeP_2,[4] demonstrated excellent catalytic activity in comparison with their pure-phase counterparts. However, the different foreign components may increase the system complexity and there is a limited choice of appropriate components. The potential of heterostructured nickel phosphide polymorphs has been demonstrated toward HER. For example, Liu et al. prepared Ni_2P-NiP_2 polymorphs via phosphatizing NiS_2 with optimal H* adsorption energy and enhanced electronic conductivity, therefore delivering improved performance in comparison with pure-phased metal phosphide.[13] Wang and co-workers proposed the water-induced formation of Ni_2P-$Ni_{12}P_5$ interfaces to regulate the electronic states and the obtained catalyst achieves a current density of 10 mA cm^{-2} with an overpotential of 76 mV.[17] To date, the controllable preparation of nickel phosphide polymorphs with desirable nanostructure and intrinsically high activity remains scientifically intriguing.

Herein, we show a heterostructured $Ni_2P/Ni_{12}P_5$ catalyst for promoting HER in alkaline electrolyte and AEM electrolyzer applications. We further dope vanadium (V) into the heterostructured nickel phosphide polymorphs to regulate the electronic structure and improve the intrinsic HER activity. With low electronegativity and abundant vacant d orbitals, vanadium has shown to be a promising doping element to form strong chemical bonding with host materials.[18–20] By taking advantage of both heteroatom doping and strong interfacial coupling between Ni_2P and $Ni_{12}P_5$, the V-doped $Ni_2P/Ni_{12}P_5$ catalyst (denoted: V-$Ni_2P/Ni_{12}P_5$) exhibits excellent catalytic performance in alkaline HER. Density functional theory (DFT) studies further confirm the important role of V-doping and heterointerfaces in regulating the water dissociation energy and the adsorption strength of hydrogen intermediates on V-$Ni_2P/Ni_{12}P_5$ heterostructured catalysts. Using the V-$Ni_2P/Ni_{12}P_5$ in a membrane electrode assembly (MEA) for an AEM electrolyzer, the cell can deliver a current density of 500 mA cm^{-2} at low cell voltages of 1.79 V with prolonged stability.

2. Results and Discussion

2.1. Synthesis and Physical Characterization

The preparation of V-$Ni_2P/Ni_{12}P_5$ heterostructured hydrogen evolution reaction electrocatalyst involves a two-step process (**Scheme 1**). First, the thin NiV hydroxide nanosheets with the precise controlled V-doping amount were grown on nickel foam (NF) through a facile hydrothermal method. Then, the prepared Ni_3V hydroxide was phosphorized in the tube furnace using $NaH_2PO_2 \cdot H_2O$ as the phosphorous source to obtain V–$Ni_2P/Ni_{12}P_5$ electrocatalysts. It was noted that the heterostructured nickel phosphide polymorphs were only obtained when the Ni_3V hydroxide and phosphorus source were placed in the same crucible. Otherwise, pure-phase nickel phosphide was obtained if placed apart (denoted: V-Ni_2P). The fabricated V-$Ni_2P/Ni_{12}P_5$ electrode with NiV precursors with a molar ratio of Ni:V equal to 3:1 shows the highest HER activity and was discussed in the following sections unless otherwise stated.

The phase structure of the samples was characterized by X-ray diffraction (XRD). As shown in **Figure 1**a, the XRD pattern of V-$Ni_2P/Ni_{12}P_5$ agrees with the component of Ni_2P (ICDD: 03-065-3544) and $Ni_{12}P_5$ (ICDD: 03-065-1623), indicating a phase restructuring process occurred and two types of nickel polymorphs were evolved during the phosphorization treatment. The strong peaks at 44.3° and 52.1° belong to the underlying NF substrate (ICDD: 03-065-2865). For comparison purposes, pure $Ni_2P/Ni_{12}P_5$ was also fabricated. Compared to pure $Ni_2P/Ni_{12}P_5$, the incorporation of V leads to a broadened XRD pattern of Ni_2P and $Ni_{12}P_5$, indicating that V doping has a great influence on the crystal structure, resulting in decreased crystallinity and increased lattice distortion.[21] The comparison between the XRD patterns of V-$Ni_2P/Ni_{12}P_5$ and V-Ni_2P demonstrates the crucial role of calcination conditions in the precise control of crystalline phases.

Scanning electron microscopy (SEM) image shows that dense NiV hydroxide nanosheets grow uniformly on the NF

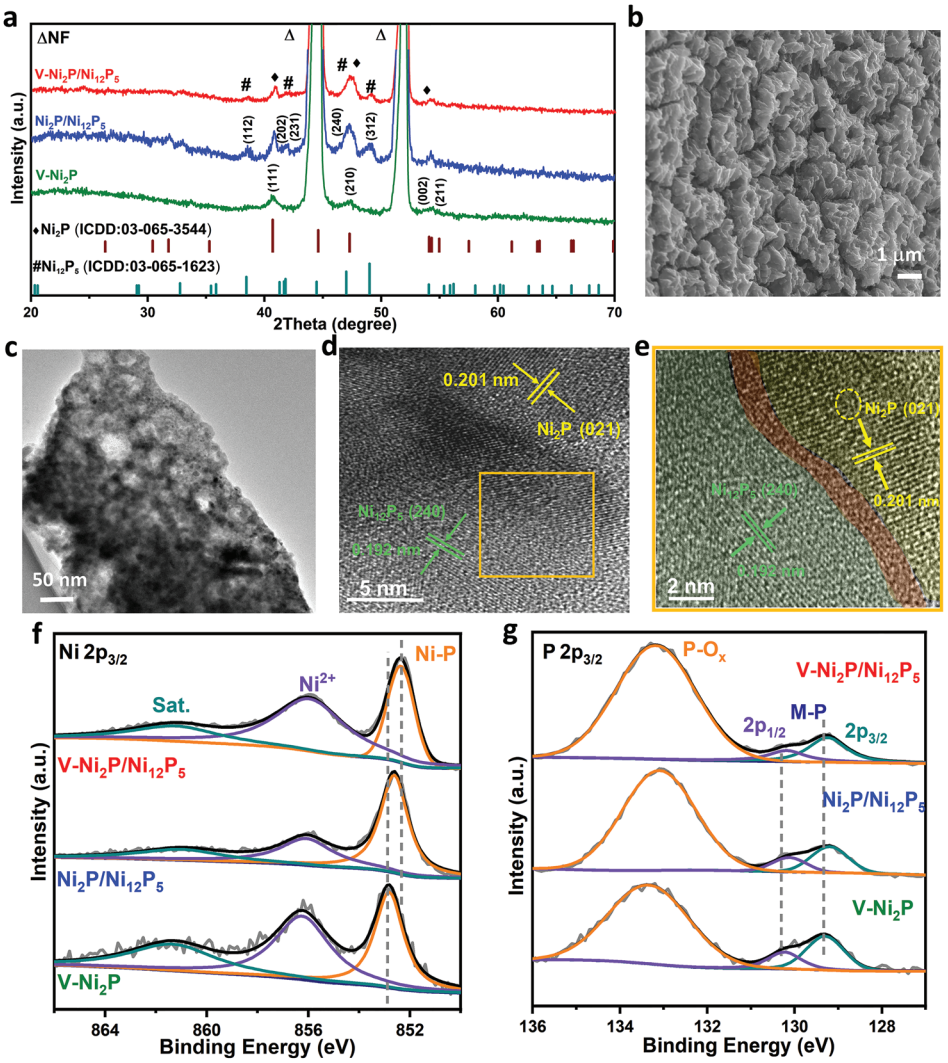

Figure 1. a) XRD patterns of V–$Ni_2P/Ni_{12}P_5$ and control samples. Characterization of the optimal V–$Ni_2P/Ni_{12}P_5$, b) SEM image and c) TEM image, d) HRTEM image and e) Enlarged HRTEM image at the interface region marked by yellow square in (d); High-resolution XPS spectra of f) Ni $2p_{3/2}$ and g) P 2p in V–$Ni_2P/Ni_{12}P_5$, $Ni_2P/Ni_{12}P_5$, and pure-phase V-Ni_2P.

skeleton (Figure S1a, Supporting Information). The subsequent phosphorization treatment has no significant influence on the morphology of V-Ni_2P, except the smooth nanosheet surface becomes roughened (Figure S1b, Supporting Information). However, the morphology of V-$Ni_2P/Ni_{12}P_5$ is completely different from those of NiV hydroxide and V-Ni_2P samples, where the nanosheets fuse into irregular interconnected nanoplate clusters with a loose and fluffy porous morphology (Figure 1b). The above morphology changes on V-$Ni_2P/Ni_{12}P_5$ are confirmed by the transmission electron microscopy (TEM) characterization, where a porous structure was observed (Figure 1c), suggesting the impact of calcination conditions in altering the morphology. Additionally, the morphology of directly phosphating $Ni(OH)_2$ without the incorporation of V dopant was also investigated ($Ni_2P/Ni_{12}P_5$), where the nanosheet structure is completely transformed into a rugged structure without specific morphology (Figure S1c). Additionally, high-resolution TEM (HRTEM) was employed to study the crystal structures of V–$Ni_2P/Ni_{12}P_5$ and the interface between the two phases (Figure 1d,e). The lattice fringes with spacings of 0.192 nm and 0.201 nm correspond to the (240) and (021) planes of $Ni_{12}P_5$ and Ni_2P, respectively. This result demonstrates the formation of phase interfaces between $Ni_{12}P_5$ and Ni_2P.[17,22] Moreover, the lattice fringes become vague near the interface, suggesting the misarrangement of atoms at the interface.[17] The energy dispersive spectroscopy (EDS) mapping results demonstrate the uniform distribution of Ni, V, and P elements throughout the V-$Ni_2P/Ni_{12}P_5$ catalyst (Figure S2, Supporting Information).

The chemical oxidation states of Ni, V, and P in the V–$Ni_2P/Ni_{12}P_5$ and the control samples are investigated by X-ray photoelectron spectroscopy (XPS). Three peaks are observed in the high-resolution Ni $2p_{3/2}$ spectrum (Figure 1f). The appearance of $Ni^{\delta+}$ at 852.4 eV corresponds to the Ni-P bond, along with surface oxidized Ni species due to the exposure of metal phosphide to air, confirming the formation of nickel phosphides.[21] Especially, compared to the $Ni_2P/Ni_{12}P_5$ sample, the binding

energy of the Ni–P peak in V–$Ni_2P/Ni_{12}P_5$ experiences a negative shift of 0.2 eV, suggesting an accumulated electron around Ni atoms and modulated electronic structure by V doping. Such partially charged species have been demonstrated to play an important role in accelerating the HER performance.[23] Additionally, in comparison with the pure-phase V–Ni_2P sample, a more negatively-shifted Ni-P binding energy was observed in the Ni $2p_{3/2}$ of the V–$Ni_2P/Ni_{12}P_5$ sample, indicating the strong electronic interactions at the $Ni_2P/Ni_{12}P_5$ interface.[4] In contrast, the P 2p spectrum of V–$Ni_2P/Ni_{12}P_5$ shows the binding energies at 129.3 and 130.2 eV for P $2p_{3/2}$ and P $2p_{1/2}$, attributing to the Ni-P bond, which is positively shifted in comparison with counterparts (Figure 1g). These results suggest a strong electronic coupling around the V-doped $Ni_2P/Ni_{12}P_5$ interface, where the electrons are transferred from P atoms to Ni atoms.[14] In the V $2p_{3/2}$ spectrum of V-$Ni_2P/Ni_{12}P_5$ (Figure S3a, Supporting Information), it shows the presence of two peaks at 516.3 eV (V^{4+}) and 517.5 eV (V^{5+}) on the electrode surface.[20] The P–O_x peak at ≈133.5 eV is also observed, originating from the surface oxidation due to air exposure. The above XPS results suggest the incorporation of V dopant and the formation of abundant heterointerfaces lead to an optimized electronic configuration with higher electron distribution at Ni sites, which can be beneficial to improving the intrinsic catalytic activity (see below).

2.2. Evaluation of Electrocatalytic Performance

The electrocatalytic HER performance of V–$Ni_2P/Ni_{12}P_5$ was evaluated using a standard three-electrode system in the 1.0 M KOH electrolyte. To optimize the catalytic activity, a series of V_x–$Ni_2P/Ni_{12}P_5$ electrodes were prepared with different amounts of V dopant. As shown in Figure S4, Supporting Information, the HER performance is improved with the increase of V dopants up to 0.25. A further increase of doping amount to 0.5 leads to a decreased HER performance, due to the damaged NF structure that is unfavorable for electron transfer and exposure to active sites (Figure S5, Supporting Information). The catalytic performance of the optimal V-$Ni_2P/Ni_{12}P_5$ electrode was further investigated, together with the counterparts of $Ni_2P/Ni_{12}P_5$, V-Ni_2P, and commercial Pt/C (20 wt.%) drop-casted onto NF. The *i*R-compensated polarization curves in **Figure 2**a demonstrate that the V-$Ni_2P/Ni_{12}P_5$ electrode exhibits a significantly improved HER activity compared to the control samples. This result suggests the important role of V-doping and the constructed interfaces in boosting the HER kinetics. Notably, the V-$Ni_2P/Ni_{12}P_5$ electrode requires an overpotential of 62 mV to deliver a current density of –10 mA cm^{-2}, much smaller than that of $Ni_2P/Ni_{12}P_5$ (95 mV), V-Ni_2P (125 mV), and bare NF (206 mV). Moreover, a lower overpotential of 146 mV is required for the V-$Ni_2P/Ni_{12}P_5$ electrode to reach -100 mA cm^{-2} (Figure 2b). In contrast, larger overpotentials are required for the $Ni_2P/Ni_{12}P_5$ (203 mV) and V-Ni_2P (248 mV) electrodes to deliver the same current density. The performance of the V-$Ni_2P/Ni_{12}P_5$ hybrid electrode is comparable to or outperforms most recently reported metal phosphides-based HER catalysts (Table S1, Supporting Information).

To verify the role of V-doping and heterointerfaces in improving the HER kinetics, Tafel slopes of the as-prepared electrodes were investigated. As shown in Figure 2c, the V–$Ni_2P/Ni_{12}P_5$ electrode exhibits a small Tafel slope of 63 mV dec^{-1}, suggesting that the reaction undergoes the Volmer-Heyrovsky process.[24] The value is lower than that of $Ni_2P/Ni_{12}P_5$ (75 mV dec^{-1}) and pure-phase V–Ni_2P (89 mV dec^{-1}), indicating a faster HER kinetic is achieved. The exchange current density (j_0) value is obtained through the extrapolation of Tafel plots at the overpotential of 0 V (**Figure 3**b and Figure S6, Supporting Information). The calculated j_0 value of V–$Ni_2P/Ni_{12}P_5$ is 1.58 mA cm^{-2}, which is 1.6, 2.7, and 14.3 times larger than that of $Ni_2P/Ni_{12}P_5$, V–Ni_2P, and bare NF, further confirming the faster HER kinetics on the V–$Ni_2P/Ni_{12}P_5$ hybrid electrode.[25] The above results demonstrate that the V–$Ni_2P/Ni_{12}P_5$ electrode with abundant heterointerfaces and V doping can boost the intrinsic HER catalytic activity.

The long-term electrocatalytic stability of the V–$Ni_2P/Ni_{12}P_5$ electrode is further investigated. The V-$Ni_2P/Ni_{12}P_5$ electrode demonstrates outstanding stability during the 40 h continuous hydrogen evolution test at -50 mA cm^{-2}, and the polarization curves obtained before and after the durability measurement show no obvious decay (Figure 2d). The chemical compositions were analyzed by inductively coupled plasma optical emission spectroscopy (ICP-OES). The atomic ratios of the elements after normalization to Ni were found to be $NiV_{0.27}P_{0.68}$ and $NiV_{0.24}P_{0.63}$ before and after HER. The slight variation of chemical compositions is possibly caused by the surface corrosion of the catalysts by KOH, resulting in slightly decreased catalytic activity (Figure 2d inset). Furthermore, the XRD pattern and SEM image reveal that the crystal structure and morphology of the electrode are well maintained after the stability test (Figures S7 and S8, Supporting Information). XPS spectra show the presence of Ni, V, and P after the HER, as well as the existence of the characteristic metal-phosphide peak (Figure S3, Supporting Information). Moreover, in comparison to in those in Figure 1f, the formation of more surface nickel phosphates during HER can be observed, which is consistent with the previous studies.[26,27] By comparing the relative peak intensity, the partial Ni-P peak is merged with the Ni^{2+} peak, and the intensity of the Ni^{2+} peak increased, demonstrating partial surface oxidation during the HER process.[14] The partially oxidized surface can be ascribed to the HER mechanism under alkaline media, where the additional H_2O adsorption process is required, resulting in the locally accumulated OH^- on the surface of the catalyst.[28] The introduction of O adsorption sites leads to surface oxidation. However, the formation of the surface nickel phosphates layer can serve as a passivation layer to prevent the dissolution of inner nickel phosphide,[29] thus ensuring the favorable stability of V-$Ni_2P/Ni_{12}P_5$.

2.3. Electronic Structure and Activity Analysis

To understand the origin of the improved performance of the V–$Ni_2P/Ni_{12}P_5$ electrode toward HER, we first evaluated the charge transfer process of these electrodes by electrochemical impedance spectroscopy (EIS). It shows that both Vdoping and constructed heterointerfaces can improve the electron transfer during HER (Figure 3a). The fitting of Nyquist plots using an equivalent circuit model (Figure S9, Supporting

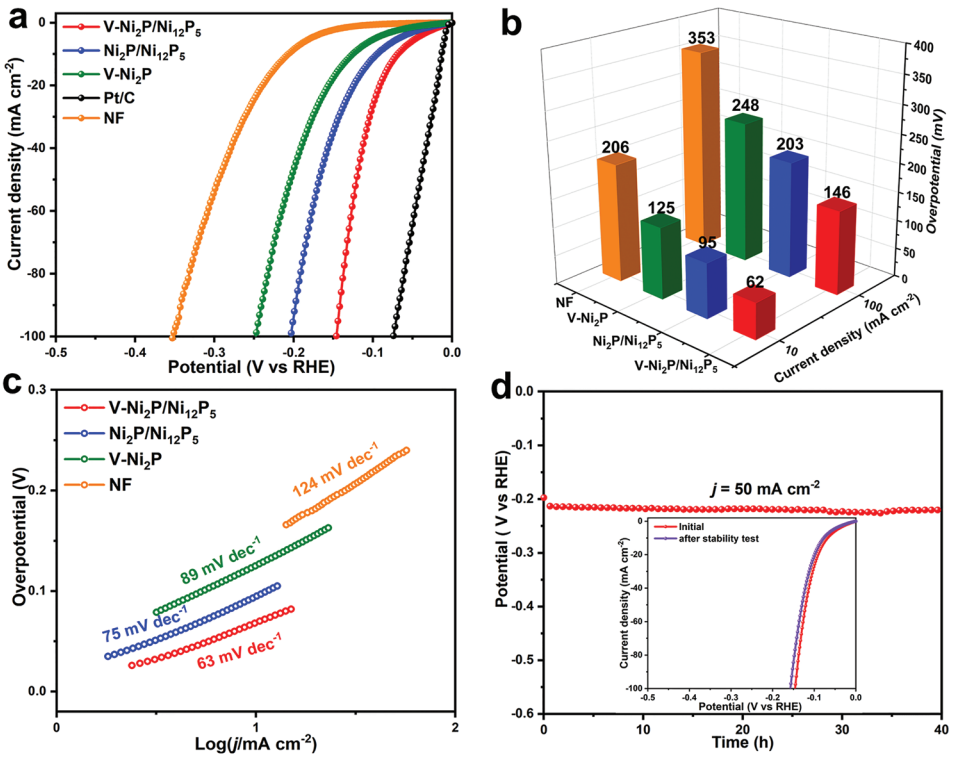

Figure 2. a) *i*R-compensated HER polarization curves, b) Comparison of overpotentials to deliver -10 and -100 mA cm^{-2} current density, c) Tafel plots of different electrodes in 1.0 M KOH. d) Long-term durability test of V-$Ni_2P/Ni_{12}P_5$ electrode and polarization curves before and after the stability test (inset).

Information) reveals the charge transfer resistance (R_{ct}) of the V–$Ni_2P/Ni_{12}P_5$ electrode (R_{ct} = 4.7 Ω) is much smaller than that of $Ni_2P/Ni_{12}P_5$ (R_{ct} = 7.8 Ω) and V–Ni_2P (R_{ct} = 9.2 Ω), suggesting a faster electron transfer kinetic of HER at the V-doped $Ni_2P/Ni_{12}P_5$ electrode.[14] Besides, the formation of abundant heterointerfaces between the two nickel phosphide polymorphs is more important for accelerating the charge transfer, as smaller charge transfer resistances were found for the samples with abundant heterointerfaces. Additionally, the electrochemical surface area (ECSA) was measured by the double-layer capacitance (C_{dl}) using cyclic voltammetry at different scan rates in a non-Faradaic region (Figure S10, Supporting Information).[30] As shown in Figure 3b, the V–$Ni_2P/Ni_{12}P_5$ electrode displays the largest ECSA among the tested samples, suggesting it possesses more catalytic active sites. Two main factors contribute to the enhanced ECSA. First, V–$Ni_2P/Ni_{12}P_5$ exhibits a loose and fluffy morphology, which is beneficial for enlarging the surface area with exposure to more active sites. Additionally, V–$Ni_2P/Ni_{12}P_5$ has a porous structure that can be seen in the TEM image, resulting in a larger ECSA. To exclude the effect from the surface area, the current density was normalized to ECSA (Figure S11, Supporting Information). Evidently, the V–$Ni_2P/Ni_{12}P_5$ electrode still exhibits a larger current density than $Ni_2P/Ni_{12}P_5$ and V-Ni_2P, revealing the enhanced intrinsic activity of each active site. Moreover, the average turnover frequencies (TOFs), which also reflect the intrinsic activity of each active site, are calculated on V–$Ni_2P/Ni_{12}P_5$, $Ni_2P/Ni_{12}P_5$, and V–Ni_2P electrodes. The number of active sites and TOFs were examined by the reported electrochemical characterizations method (Figure S12, Supporting Information).[31,32] The TOF of V–$Ni_2P/Ni_{12}P_5$ at the overpotential 100 mV is calculated to be 0.18 s^{-1}, which is higher than that of $Ni_2P/Ni_{12}P_5$ (0.1 s^{-1}) and V–Ni_2P (0.088 s^{-1}), further verifying the promoted HER intrinsic activity on the V–$Ni_2P/Ni_{12}P_5$ electrode. Based on the electrochemical results, it can be concluded that the boosted HER performance is mainly attributed to the excellent intrinsic activity as well as the enlarged electrochemical surface area.

To obtain insights into the specific active sites of V–$Ni_2P/Ni_{12}P_5$ for HER, the thiocyanate ions (SCN^-) were introduced into the electrolyte, which is known to efficiently interact with metal and poison metal-centered active sites.[33–35] As shown in Figure 3c, upon the addition of SCN^-, the HER current of the V–$Ni_2P/Ni_{12}P_5$ electrode decreased dramatically, confirming the HER activity dominantly derives from the metal sites (Ni–V bridge sites, see below). For the control sample $Ni_2P/Ni_{12}P_5$, similar to the V–$Ni_2P/Ni_{12}P_5$ electrode, the HER current of the $Ni_2P/Ni_{12}P_5$ electrode also substantially decreased with the addition of SCN^- (Figure S13, Supporting Information). In contrast, the V-Ni_2P electrode only experiences a slight drop in HER activity in SCN^- containing solution. These results suggest that for the pure-phase V–Ni_2P, the dissociated proton tends to adsorb on the P sites, due to the negatively charged P sites would potentially bond with the proton and served as the main active sites during HER.[13,36,37] While for the heterostructured V–$Ni_2P/Ni_{12}P_5$ and $Ni_2P/Ni_{12}P_5$ samples, the electron redistribution at the interfaces would change the main active sites from P sites to the metal bridge sites.

In situ Raman spectroscopy was further employed to capture the reaction intermediates of V–$Ni_2P/Ni_{12}P_5$ and gain insights into the HER mechanism. The measurements were performed

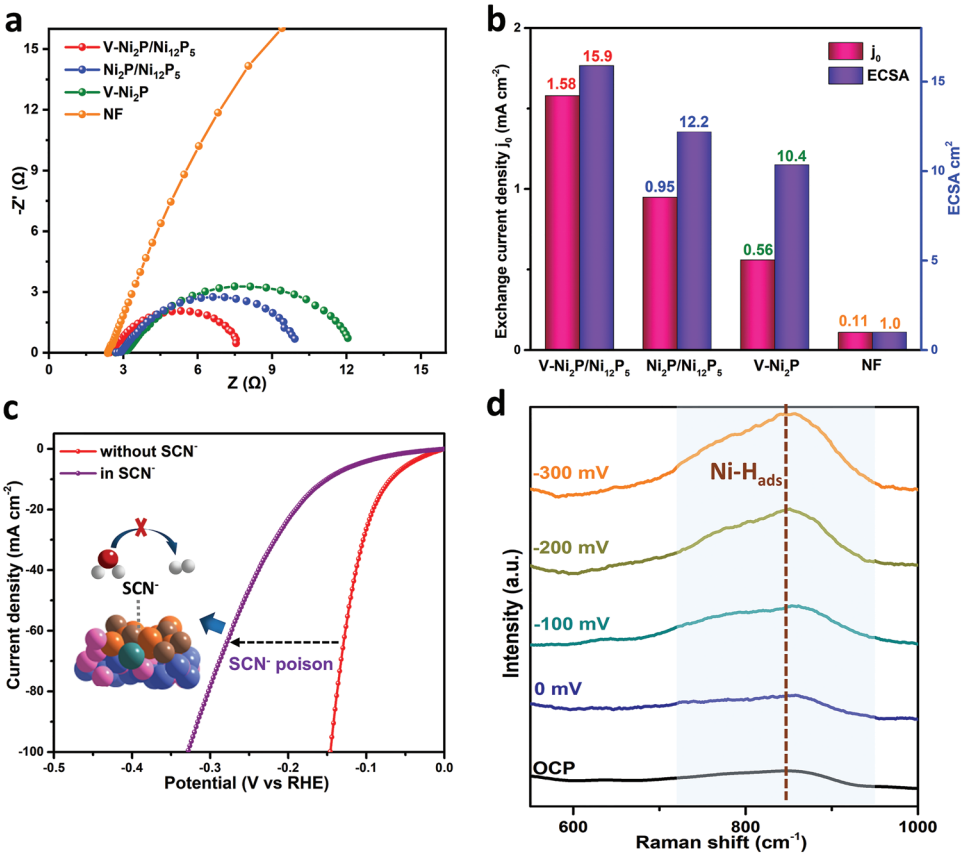

Figure 3. a) Nyquist plots of V–$Ni_2P/Ni_{12}P_5$ and counterparts measured at an overpotential of 233 mV. b) Exchange current density (red) and ECSA (purple) of as-prepared electrodes. c) HER polarization curves of V–$Ni_2P/Ni_{12}P_5$ with and without 10 mM KSCN in 1.0 M KOH, demonstration of metal sites is blocked by SCN^- (inset). d) In situ Raman spectra of V-$Ni_2P/Ni_{12}P_5$ at OCP and different applied potentials versus RHE.

with a Teflon in situ Raman cell, and the as-prepared electrodes, gold wire, and saturated calomel electrode were used as a working electrode, counter electrode, and reference electrode, respectively (Figure S14a, Supporting Information). The in situ Raman spectra were collected at a potential range from the open circuit potential (OCP) to −300 mV versus reversible hydrogen electrode (RHE). As shown in Figure 3d, no obvious peak was detected at OCP and 0 mV vs RHE. When the applied potentials were above −100 mV versus RHE, a broad peak centered at 845 cm^{-1} appeared, which is attributed to a Ni–H_{ads} vibrational band.[38,39] The peak intensity increases when more negative potentials were applied (from −100 mV to −300 mV vs RHE), suggesting that Ni–H_{ad} intermediate species were formed on the catalyst during the HER. In contrast, no such peak was observed when the same potential was applied to the V–Ni_2P electrode (Figure S14b, Supporting Information). The above experimental results demonstrate the metal sites in the heterostructured V–$Ni_2P/Ni_{12}P_5$ are the major catalytic active sites for HER.

2.4. Theoretical Simulations

Density functional theory (DFT) calculations were further carried out to understand the alkaline HER activity of the V–$Ni_2P/Ni_{12}P_5$ catalyst. Here, we consider the three main processes in alkaline HER, including adsorption of H_2O molecules, H_2O dissociation, and the adsorption/desorption of hydrogen intermediate (H*). Firstly, the optimized adsorption structure of H* and OH* adsorption on the surface of V–$Ni_2P/Ni_{12}P_5$, $Ni_2P/Ni_{12}P_5$, and V–Ni_2P is shown in **Figure 4**a and Figure S15, Supporting Information. It is known that the HER is strongly affected by the adsorbed H_2O molecules because the weak adsorption of H_2O on the catalyst leads to a higher energy barrier for the H_2O dissociation step.[14,40] As shown in Figure S16a, Supporting Information, the V–$Ni_2P/Ni_{12}P_5$ surface has the lowest H_2O adsorption energy (ΔG_{H_2O}) value of –0.93 eV in comparison to $Ni_2P/Ni_{12}P_5$ (–0.61 eV) and V–Ni_2P (–0.31 eV), demonstrating that V-doped $Ni_2P/Ni_{12}P_5$ surface is more energetically favorable for H_2O adsorption, and thus benefiting for the Volmer process.[31]

Then, the energy barrier required for H_2O dissociation and adsorption of H* is calculated for evaluating the HER catalytic performance.[22] The calculated results of the H_2O dissociation diagram show a large energy barrier of 1.34 eV on the V–Ni_2P surface (Figure S16b, Supporting Information), which greatly hinders the water dissociation to form H*, resulting in sluggish HER kinetics. The H_2O dissociation energy barrier is reduced to 0.90 eV on the $Ni_2P/Ni_{12}P_5$ surface and further reduced to 0.52 eV on the V–$Ni_2P/Ni_{12}P_5$ surface. These results suggest the

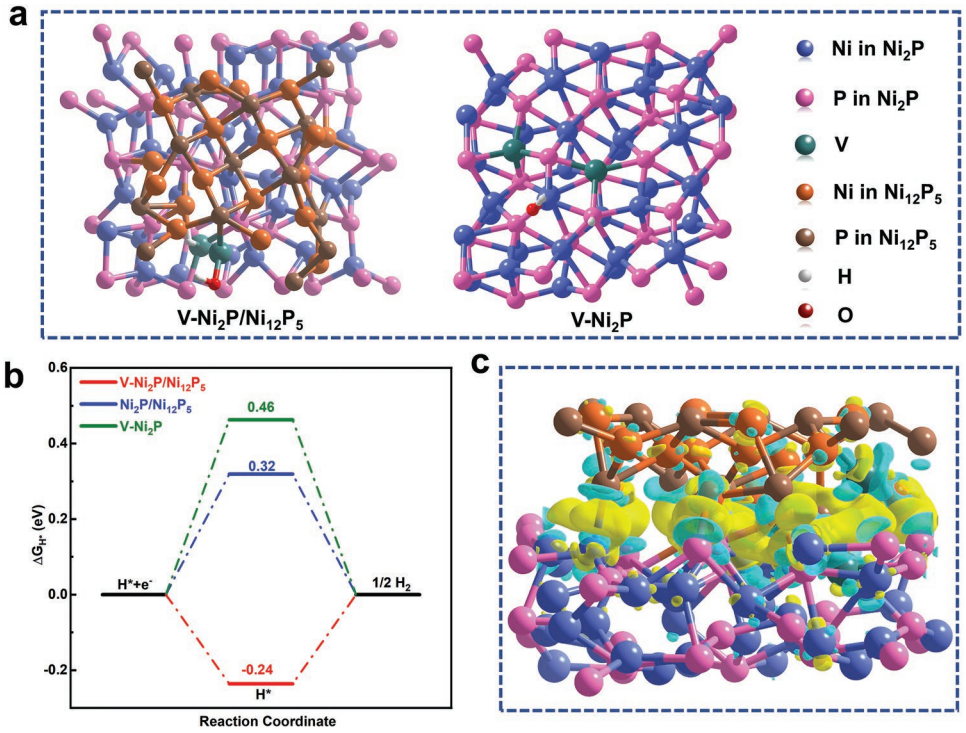

Figure 4. a) The optimized calculation models of adsorption of H* and OH* intermediates on V-$Ni_2P/Ni_{12}P_5$ and V-Ni_2P (top view). b) HER free energy diagram calculated for different electrode materials. c) Calculated charge density distribution at the interface. Yellow and cyan refer to electron-rich and electron-deficient areas, respectively.

important role of the constructed $Ni_2P/Ni_{12}P_5$ interfaces and V doping in promoting the dissociation of H_2O molecules to form H* intermediates.[16] For the pure-phase V–Ni_2P catalyst, the H* tends to adsorb on a P site, which is in accordance with the literature.[13,14] In contrast, for the V–$Ni_2P/Ni_{12}P_5$ catalyst, the dissociated H* tends to adsorb on the Ni–V bridge sites at the interface, and the V sites in $Ni_{12}P_5$ near the phase junction exhibits a higher affinity for the OH group (Figure 4a).

As evident by both theoretical calculations and experimental results, the formation of heterointerfaces would change the proton-acceptor from P atoms to the Ni–V bridge sites near the phase junction. The calculated free energies of hydrogen (ΔG_{H^*}) on V–$Ni_2P/Ni_{12}P_5$, $Ni_2P/Ni_{12}P_5$, and V–Ni_2P with the most energetically stable configurations are calculated, and the V–$Ni_2P/Ni_{12}P_5$ catalyst displays a value of ΔG_{H^*} (–0.24 eV) at the interface region (Figure 4b), which is smaller than those on pure-phase V–Ni_2P (0.46 eV) and $Ni_2P/Ni_{12}P_5$ (0.32 eV). The decreased $|\Delta G_{H^*}|$ value for V–$Ni_2P/Ni_{12}P_5$ catalyst indicates the synergistic effects of interfacial interactions and V-doping on optimizing the adsorption of H*. In this way, the subsequent H_2 generation process will also be accelerated, thanks to the optimal binding energy between H* and catalyst surfaces.

To gain insights into the aforementioned effects of the heterointerface and V-doping on H* binding, the charge distribution of Ni and P atoms at the interface was investigated using Bader charge analysis (Table S2, Supporting Information).[18] Substantial electrons are accumulated at the interfacial region in comparison with the region away from the interface (Figure 4c), indicating a clear electron redistribution at the interface. According to the calculation results, the formation of heterostructure and V-doping leads to ≈0.023 electrons per atom migrating from the $Ni_{12}P_5$ phase to the Ni_2P phase and accumulating at Ni atoms in Ni_2P close to the interface. Simultaneously, P atoms of V–Ni_2P at the interface lose electrons (≈0.034 electrons per atom). Such electronic transfer between the two components is beneficial for the interactions of reactants with the catalyst surface, thereby improving the interfacial reactivity of the hybrid structure.[14] The above DFT results suggest that the V-doped nickel phosphide polymorphs can effectively regulate the water dissociation behavior of H_2O molecules, the adsorption energy of H* intermediates as well as the release of H_2. The strong coupling interactions between the two phases and the optimized electronic structure by V-doping, synergistically accelerate the reaction kinetics and electrochemical performance in HER.

2.5. Application for AEM Water Electrolyzer

To demonstrate the potential of V-$Ni_2P/Ni_{12}P_5$ catalysts for large current density water electrolysis, an AEM electrolyzer was constructed by coupling the as-prepared V-$Ni_2P/Ni_{12}P_5$ (cathode) with a NiFeCr layered double hydroxide (LDH, anode)[41] (**Figure 5**a). NiFeCr LDH is selected as an anode material because it exhibits outstanding OER activity (Figure S17, Supporting Information), and it represents the benchmark transition-metal-based OER catalysts.[42–44] The AEM electrolyzer (NiFeCr‖V-$Ni_2P/Ni_{12}P_5$) was tested at room temperature and 55 °C, respectively (Figure S18, Supporting Information). Increasing electrolyte temperature significantly decreases cell

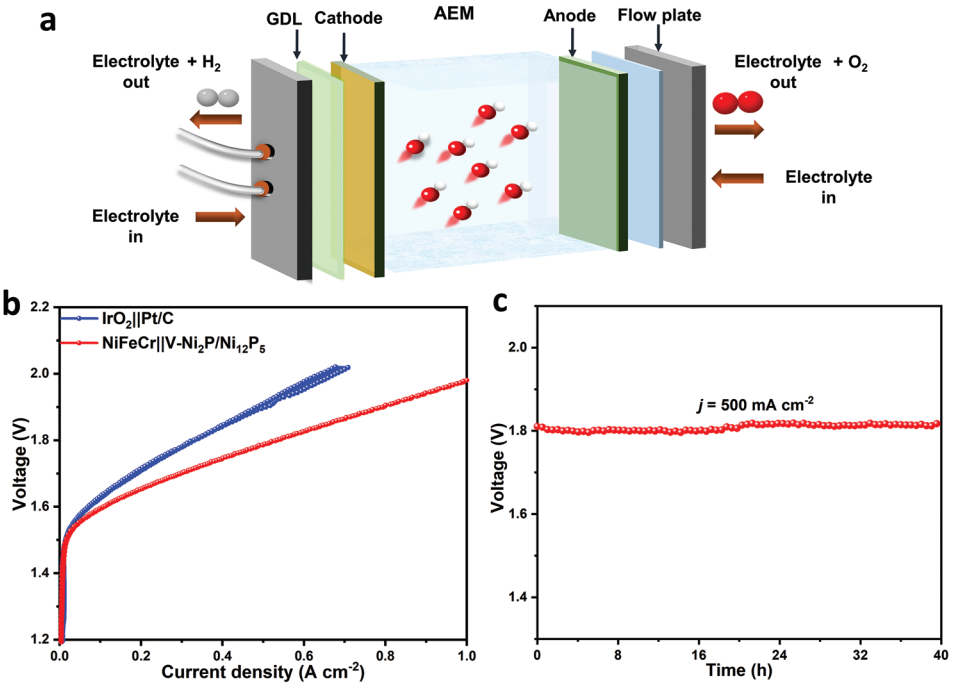

Figure 5. a) Schematic representation for an AEM electrolyzer. b) Polarization curves of NiFeCr‖V-$Ni_2P/Ni_{12}P_5$ and commercial IrO_2‖(Pt/C) AME electrolyzer recorded at 55 °C in 1.0 M KOH solution (without *i*R compensation). c) Chronopotentiometric curve of the NiFeCr‖V-$Ni_2P/Ni_{12}P_5$ AME electrolyzer at the cell density of 500 mA cm^{-2}.

voltage. For example, the NiFeCr‖V-$Ni_2P/Ni_{12}P_5$ cell delivers up to 400 mA cm^{-2} at a cell voltage of 2.0 V at room temperature, while the same current density can be obtained at 1.73 V at 55 °C. In comparison to an AEM electrolyzer made from commercial catalysts IrO_2‖(Pt/C) at 55 °C (Figure 5b). The NiFeCr‖V–$Ni_2P/Ni_{12}P_5$ cell delivers a current density of 500 mA cm^{-2} at the cell voltage of 1.79 V, corresponding to an energy conversion efficiency of 70%, while the IrO_2‖(Pt/C) cell requires 1.91 V to deliver the same current density, corresponding to the energy efficiency of 63%.

The Faradaic efficiency (FE) of the AEM water electrolyzer was evaluated by collecting the evolved gaseous products over the cathode at a cell voltage of 1.7 V via gas chromatography (GC). The average FE of 98.9% was detected when employing the V–$Ni_2P/Ni_{12}P_5$ cathode in the AEM electrolysis (Figure S19, Supporting Information). This result suggests the generation of pure H_2 without any undesirable side reactions in our AEM water electrolyzer. The performance is comparable or superior to the state-of-art AEM water electrolyzers reported using transition metal-based electrodes (Table S3, Supporting Information). Furthermore, the long-term stability of the NiFeCr‖V–$Ni_2P/Ni_{12}P_5$ cell was conducted at a constant current density of 500 mA cm^{-2} for 40 h. No significant voltage increase was observed (Figure 5c), demonstrating its great potential for future practical water electrolysis.

3. Conclusions

A V-$Ni_2P/Ni_{12}P_5$ heterostructured electrocatalyst has been developed for robust hydrogen production. As confirmed by experimental and DFT calculation results, the strong interactions between two nickel phosphide polymorphs and V dopants endow V–$Ni_2P/Ni_{12}P_5$ with optimized electronic configuration, large electrochemical surface areas with more exposed active sites, fast reaction kinetics, and enhanced electrical conductivity, thus enabling excellent HER activity and robust durability in alkaline media. The electron redistribution around the heterointerfaces in the hybrid catalyst promotes adsorption and dissociation of water molecules as well as optimizing the binding energy of H* intermediates on the catalytic active sites. When applied in an AEM water electrolyzer, the catalyst demonstrated satisfying performance, further highlighting its potential application for large-scale hydrogen production. This work provides a strategy to enhance the catalytic performance of transition metal-based electrocatalysts by regulating the electronic structure and intrinsic activity.

4. Experimental Section

Synthesis of $Ni_{1-x}V_x$ Precursors: Ni foam (NF, 2 × 3 cm, 1.5 mm thickness) was sequentially sonicated in 3.0 M HCl and deionized (DI) water for 15 min to remove the surface oxide. The NiV electrode was prepared by a hydrothermal method. In brief, the desired amount of $NiCl_2{\cdot}6H_2O$, $VCl_3{\cdot}6H_2O$, 6 mmol of urea, and 4 mmol of NH_4F were dissolved in 40 mL DI water with vigorous stirring for 30 min. The total amount of metal ions was kept at 3 mmol, and different molar ratios of Ni:V (Ni:V equals 1:0, 12:1, 3:1, and 1:1) were used to prepare the NiV electrode. Afterward, the above solution was transferred into a 25 mL Teflon-lined stainless-steel autoclave and heated at 120 °C for 12 h. The as-prepared materials were rinsed with DI water and dried at 60 °C.

Synthesis of V-$Ni_2P/Ni_{12}P_5$ Electrodes: The as-prepared $Ni_{1-x}V_x$ precursor was mixed with different amounts of $NaH_2PO_2{\cdot}H_2O$ and

put into a crucible with a cover. The crucible was placed at the center of the tube furnace and annealed at 350 °C for 60 min with a rising rate of 2 °C min^{-1} under Ar atmosphere. After being cooled down, the final product was collected by rinsing with DI water several times and vacuum drying. The mass loading is ≈2.0 mg cm^{-2}.

Supporting Information

Supporting Information is available from the Wiley Online Library or from the author.

Acknowledgements

The study was supported by the Australian Renewable Energy and Australian Research Council (FT170100224, DP210103892, and IC200100023). The authors thank the Mark Wainwright Analytical Center (MWAC) at the University of New South Wales for providing the physical characterization instruments. The authors acknowledge the support from Tsinghua National Laboratory for Information Science and Technology for theoretical simulations

Open access publishing facilitated by University of New South Wales, as part of the Wiley - University of New South Wales agreement via the Council of Australian University Librarians.

Conflict of Interest

The authors declare no conflict of interest.

Data Availability Statement

The data that support the findings of this study are available from the corresponding author upon reasonable request.

Keywords

anion exchange membrane (AEM) electrolyzers, active sites, elemental doping, heterointerfaces, hydrogen evolution reaction, metal phosphides

Received: August 3, 2022
Published online: September 4, 2022

[1] Y. Wang, B. Liu, X. Shen, H. Arandiyan, T. Zhao, Y. Li, M. Garbrecht, Z. Su, L. Han, A. Tricoli, C. Zhao, *Adv. Energy Mater.* **2021**, *11*, 2003759.
[2] J. Lee, H. Jung, Y. S. Park, N. Kwon, S. Woo, N. C. S. Selvam, G. S. Han, H. S. Jung, P. J. Yoo, S. M. Choi, J. W. Han, B. Lim, *Appl. Catal., B* **2021**, *294*, 120246.
[3] N. Ul Hassan, M. Mandal, G. Huang, H. A. Firouzjaie, P. A. Kohl, W. E. Mustain, *Adv. Energy Mater.* **2020**, *10*, 2001986.
[4] A. Kumar, V. Q. Bui, J. Lee, A. R. Jadhav, Y. Hwang, M. G. Kim, Y. Kawazoe, H. Lee, *ACS Energy Lett.* **2021**, *6*, 354.
[5] Z. Zhang, C. Jiang, P. Li, K. Yao, Z. Zhao, J. Fan, H. Li, H. Wang, *Small* **2021**, *17*, 2007333.
[6] A. Morozan, H. Johnson, C. Roiron, G. Genay, D. Aldakov, A. Ghedjatti, C. T. Nguyen, P. D. Tran, S. Kinge, V. Artero, *ACS Catal.* **2020**, *10*, 14336.
[7] L. Zhai, T. W. Benedict Lo, Z.-L. Xu, J. Potter, J. Mo, X. Guo, C. C. Tang, S. C. Edman Tsang, S. P. Lau, *ACS Energy Lett.* **2020**, *5*, 2483.
[8] G. Wang, W. Chen, G. Chen, J. Huang, C. Song, D. Chen, Y. Du, C. Li, K. K. Ostrikov, *Nano Energy* **2020**, *71*, 104637.
[9] L. Xiong, B. Wang, H. Cai, H. Hao, J. Li, T. Yang, S. Yang, *Appl. Catal., B* **2021**, *295*, 120283.
[10] G. Yuan, J. Bai, L. Zhang, X. Chen, L. Ren, *Appl. Catal., B* **2021**, *284*, 119693.
[11] X. Wu, Z. Wang, D. Zhang, Y. Qin, M. Wang, Y. Han, T. Zhan, B. Yang, S. Li, J. Lai, L. Wang, *Nat. Commun.* **2021**, *12*, 4018.
[12] D. Zhang, H. Miao, X. Wu, Z. Wang, H. Zhao, Y. Shi, X. Chen, Z. Xiao, J. Lai, L. Wang, *Chinese J. Catal.* **2022**, *43*, 1148.
[13] T. Liu, A. Li, C. Wang, W. Zhou, S. Liu, L. Guo, *Adv. Mater.* **2018**, *30*, 1803590.
[14] Q. Fu, X. Wang, J. Han, J. Zhong, T. Zhang, T. Yao, C. Xu, T. Gao, S. Xi, C. Liang, L. Xu, P. Xu, B. Song, *Angew. Chem., Int. Ed.* **2021**, *60*, 259.
[15] C. Liu, T. Gong, J. Zhang, X. Zheng, J. Mao, H. Liu, Y. Li, Q. Hao, *Appl. Catal., B* **2020**, *262*, 118245.
[16] Y. Li, X. Tan, H. Tan, H. Ren, S. Chen, W. Yang, S. C. Smith, C. Zhao, *Energy Environ. Sci.* **2020**, *13*, 1799.
[17] Z. Wang, S. Wang, L. Ma, Y. Guo, J. Sun, N. Zhang, R. Jiang, *Small* **2021**, *17*, 2006770.
[18] Y. Li, X. Tan, W. Yang, X. Bo, Z. Su, T. Zhao, S. C. Smith, C. Zhao, *Cell Rep. Phys. Sci.* **2020**, *1*, 100275.
[19] Y. Li, X. Jiang, Z. Miao, J. Tang, Q. Zheng, F. Xie, D. Lin, *ChemCatChem* **2020**, *12*, 917.
[20] Y. Li, X. Tan, R. K. Hocking, X. Bo, H. Ren, B. Johannessen, S. C. Smith, C. Zhao, *Nat. Commun.* **2020**, *11*, 2720.
[21] T. Zhao, X. Shen, Y. Wang, R. K. Hocking, Y. Li, C. Rong, K. Dastafkan, Z. Su, C. Zhao, *Adv. Funct. Mater.* **2021**, *31*, 2100614.
[22] X. Luo, P. Ji, P. Wang, R. Cheng, D. Chen, C. Lin, J. Zhang, J. He, Z. Shi, N. Li, S. Xiao, S. Mu, *Adv. Energy Mater.* **2020**, *10*, 1903891.
[23] X. Wang, C. Xu, M. Jaroniec, Y. Zheng, S.-Z. Qiao, *Nat. Commun.* **2019**, *10*, 4876.
[24] T. Zhao, Y. Wang, S. Karuturi, K. Catchpole, Q. Zhang, C. Zhao, *Carbon Energy* **2020**, *2*, 582.
[25] J. Duan, S. Chen, C. A. Ortíz-Ledón, M. Jaroniec, S.-Z. Qiao, *Angew. Chem., Int. Ed.* **2020**, *59*, 8181.
[26] J. Zhang, Z. Zhang, Y. Ji, J. Yang, K. Fan, X. Ma, C. Wang, R. Shu, Y. Chen, *Appl. Catal., B* **2021**, *282*, 119609.
[27] J. Chang, G. Wang, Z. Yang, B. Li, Q. Wang, R. Kuliiev, N. Orlovskaya, M. Gu, Y. Du, G. Wang, Y. Yang, *Adv. Mater.* **2021**, *33*, 2101425.
[28] H. Roh, H. Jung, H. Choi, J. W. Han, T. Park, S. Kim, K. Yong, *Appl. Catal., B* **2021**, *297*, 120434.
[29] M. Ledendecker, S. Krick Calderón, C. Papp, H.-P. Steinrück, M. Antonietti, M. Shalom, *Angew. Chem., Int. Ed.* **2015**, *54*, 12361.
[30] Y. Wang, A. Sharma, T. Duong, H. Arandiyan, T. Zhao, D. Zhang, Z. Su, M. Garbrecht, F. J. Beck, S. Karuturi, C. Zhao, K. Catchpole, *Adv. Energy Mater.* **2021**, *11*, 2101053.
[31] K. Wu, K. Sun, S. Liu, W.-C. Cheong, Z. Chen, C. Zhang, Y. Pan, Y. Cheng, Z. Zhuang, X. Wei, Y. Wang, L. Zheng, Q. Zhang, D. Wang, Q. Peng, C. Chen, Y. Li, *Nano Energy* **2021**, *80*, 105467.
[32] Y. Pan, K. Sun, Y. Lin, X. Cao, Y. Cheng, S. Liu, L. Zeng, W.-C. Cheong, D. Zhao, K. Wu, Z. Liu, Y. Liu, D. Wang, Q. Peng, C. Chen, Y. Li, *Nano Energy* **2019**, *56*, 411.
[33] Y. Shi, Z.-R. Ma, Y.-Y. Xiao, Y.-C. Yin, W.-M. Huang, Z.-C. Huang, Y.-Z. Zheng, F.-Y. Mu, R. Huang, G.-Y. Shi, Y.-Y. Sun, X.-H. Xia, W. Chen, *Nat. Commun.* **2021**, *12*, 3021.
[34] C.-F. Li, J.-W. Zhao, L.-J. Xie, J.-Q. Wu, G.-R. Li, *Appl. Catal., B* **2021**, *282*, 119463.
[35] D. Zhao, K. Sun, W.-C. Cheong, L. Zheng, C. Zhang, S. Liu, X. Cao, K. Wu, Y. Pan, Z. Zhuang, B. Hu, D. Wang, Q. Peng, C. Chen, Y. Li, *Angew. Chem., Int. Ed.* **2020**, *59*, 8982.
[36] R. B. Wexler, J. M. P. Martirez, A. M. Rappe, *ACS Catal.* **2017**, *7*, 7718.
[37] J. Yu, W.-J. Li, H. Zhang, F. Zhou, R. Li, C.-Y. Xu, L. Zhou, H. Zhong, J. Wang, *Nano Energy* **2019**, *57*, 222.
[38] Z. Qiu, C.-W. Tai, G. A. Niklasson, T. Edvinsson, *Energy Environ. Sci.* **2019**, *12*, 572.

[39] Y. Li, D. M. Patel, C.-S. Tsang, R. Zhang, M. Liu, G. S. Hwang, L. Y. S. Lee, *Adv. Mater. Interfaces* **2021**, *8*, 2001665.
[40] N. Chen, Y.-X. Du, G. Zhang, W.-T. Lu, F.-F. Cao, *Nano Energy* **2021**, *81*, 105605.
[41] X. Bo, Y. Li, R. K. Hocking, C. Zhao, *ACS Appl. Mater. Interfaces* **2017**, *9*, 41239.
[42] X. Bo, R. K. Hocking, S. Zhou, Y. Li, X. Chen, J. Zhuang, Y. Du, C. Zhao, *Energy Environ. Sci.* **2020**, *13*, 4225.
[43] X. Bo, Y. Li, X. Chen, C. Zhao, *Chem. Mater.* **2020**, *32*, 4303.
[44] M. H. Wang, Z. X. Lou, X. Wu, Y. Liu, J. Y. Zhao, K. Z. Sun, W. X. Li, J. Chen, H. Y. Yuan, M. Zhu, S. Dai, P. F. Liu, H. G. Yang, *Small* **2022**, *18*, 2200303.